Meccanica
https://doi.org/10.1007/s11012-024-01862-7

RESEARCH

# Influence of extruder geometry and bio-ink type in extrusion-based bioprinting via an in silico design tool

**Francesco Chirianni · Giuseppe Vairo · Michele Marino**

Received: 21 December 2023 / Accepted: 18 July 2024


**Abstract** Planning a smooth-running and effective extrusion-based bioprinting process is a challenging endeavor due to the intricate interplay among process variables (e.g., printing pressure, nozzle diameter, extrusion velocity, and mass flow rate). *A priori* predicting how process variables relate each other is complex due to both the non-Newtonian response of bio-inks and the extruder geometries. In addition, ensuring high cell viability is of paramount importance, as bioprinting procedures expose cells to stresses that can potentially induce mechanobiological damage. Currently, in laboratory settings, bioprinting planning is often conducted through expensive and time-consuming trial-and-error procedures. In this context, an in silico strategy has been recently proposed by the authors for a clear and streamlined pathway towards bioprinting process planning (Chirianni et al. in Comput Methods Appl Mech Eng 419:116685, 2024. https://doi.org/10.1016/j.cma.2023.116685). The aim of this work is to investigate on the influence of bio-ink polymer type and of cartridge-nozzle connection shape on the setting of key process variables by adopting such in silico strategy. In detail, combinations of two different bio-inks and three different extruder geometries are considered. Nomograms are built as graphical fast design tools, thus informing how the printing pressure, the mass flow rate and the cell viability vary with extrusion velocity and nozzle diameter.

**Keywords** Bioprinting · Non-Newtonian fluid dynamics · Reduced-order modeling · Process design tools

F. Chirianni (✉) · G. Vairo · M. Marino
Department of Civil Engineering and Computer Science Engineering, University of Rome Tor Vergata, via del Politecnico 1, 00133 Rome, Italy
e-mail: chirianni@ing.uniroma2.it

G. Vairo
e-mail: vairo@ing.uniroma2.it

M. Marino
e-mail: m.marino@ing.uniroma2.it

## 1 Introduction

Bioprinting is the cutting-edge technology in the field of tissue engineering for the fabrication of artificial cell-laden constructs [1–6]. Specifically, in the realm of extrusion-based techniques [7–9], a mixture of viable cells and biomaterials, often referred to as bio-ink [10], is loaded into the printing system and then layer-by-layer squeezed out through a syringe with varying cross-sections onto a platform, building a three-dimensional construct [11].

Even with the latest advancements in bioprinting research, there are still high uncertainties when it comes to planning the bioprinting process [12–17] and choosing the optimal setting for the involved process variables [18–21]. These latter, with reference to the extrusion-based bioprinting technique, are

Published online: 25 July 2024

the printing pressure, nozzle diameter, target extrusion velocity, and/or mass flow rate, whose optimal choice is intricately tied to the specific application. These settings should fulfill technological demands (e.g., printability, process speed, resolution), as well as ensure the utmost cell viability by the end of the process [13]. Indeed, the printing process subjects cells to mechanical stresses, potentially causing damage such as the disruption of the outer cell membrane or the onset of apoptotic signals [22–24]. Specifically, the shear forces, prevailing as the bio-ink flows through the extruder nozzle [25–27], and the extensional effects resulting from extruder cross-section reductions [25, 28, 29] or occuring at the exit of the nozzle [30] can lead to cell damage phenomena.

Determining the optimal configuration of process variables for a specific application becomes even more intricate due to the non-Newtonian features of bio-inks and the non-simple geometries of the extrusion system. This complexity gives rise to intricate non-linear and coupled relationships among process variables [18, 31], often entangled in conflicting demands. For instance, while a high mass flow rate is desirable for speeding-up printing operations, it concurrently introduces elevated stresses that may compromise cell viability [32]. Then again, opting for nozzles with a smaller diameter enhances printing resolutions, but it comes with the drawback of heightened printing pressures, potentially compromising printability and elevating the risk of cell damage [13, 25–27, 33, 34]. Currently, bioprinting planning in laboratory practice primarily relies on heuristic methods, culminating in expensive and time-consuming trial-and-error attempts [31].

In this framework, the present work aims to furnish some insights on the optimal setting of process variables, starting from a recent contribute by the authors [19] to the development of a methodological approach aimed at the logical and efficient planning and execution of bioprinting procedures. In detail, the proposed approach allows to build bio-ink specific nomograms, that is easy-to-use graphical tools that synthesize the complex relationships among process variables and that enable to deliver a solution towards a more rational and efficient calibration of the printing parameters. For instance, by selecting a set of input parameters (e.g., nozzle diameter and extrusion velocity) the assessment of required printing pressure and resulting mass flow rate and cell viability is straightforward. In this work, the validity of the proposed approach is extended towards different case studies, focusing on the influence of bio-ink polymer type and of cartridge-nozzle connection shape on the key process variables.

## 2 Materials and methods

In this section, we recall the theoretical framework and the computational modeling strategies adopted in the in silico approach proposed in [19]. In Sect. 2.1 the fluid-dynamics problem associated with the bio-ink extrusion process is addressed. A metric for cell viability is provided in Sect. 2.2. Numerical aspects with regard to high-fidelity computational-fluid-dynamics (CFD) simulations are addressed in Sect. 2.3, while in Sect. 2.4 the reduced-order modeling strategy and the procedure for building the bio-ink specific nomograms are briefly traced.

### 2.1 The fluid-dynamics problem

The extrusion bioprinting process is simulated by describing the bio-ink as an incompressible, non-Newtonian viscous fluid. The latter undergoes a laminar and isothermal flow regime when subjected to an inlet–outlet pressure difference [25, 35, 36]. By assuming the problem axisymmetry, the internal flow through the extruder (cartridge and nozzle regions in Fig. 1) can be referred to a two-dimensional axisymmetric description [19].

With reference to the notation introduced in Fig. 1, let the cylindrical coordinate system $(r, \theta, z)$ be considered, with unit basis vectors $\boldsymbol{e}_r$, $\boldsymbol{e}_\theta$ and $\boldsymbol{e}_z$ and let $\Omega$ be the two-dimensional axisymmetric extruder domain. The domain boundary $\partial\Omega$ results in $\partial\Omega = \Sigma_i \cup \Sigma_w \cup \Sigma_{ax} \cup \Sigma_o$, where $\Sigma_i$, $\Sigma_w$, $\Sigma_{ax}$ and $\Sigma_o$ refer, respectively, the inflow cross-section of the cartridge, the rigid wall (interesting both cartridge and nozzle contiguous regions), the symmetry axis of the extrusion domain (being coincident with the $z$-axis) and the outflow cross-section of the nozzle.

By disregarding any effect induced by volume forces and by adopting the five-parameter Carreau-Yasuda model [37, 38] to describe the non-Newtonian rheological behaviour, the steady-state response of the bio-ink is governed, in terms of the axisymmetric velocity

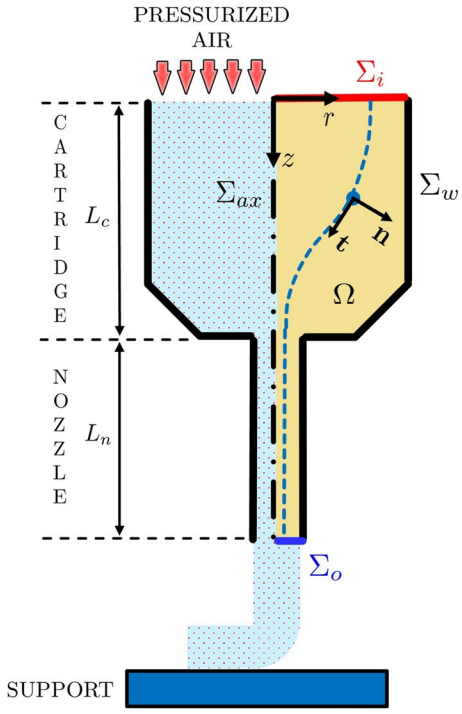


**Fig. 1** Schematic representation of the extrusion process and of the two-dimensional axisymmetric description

field $v(r, z) = v_r \boldsymbol{e}_r + v_z \boldsymbol{e}_z$ and pressure field $p(r, z)$, by the following differential problem:

$$\nabla \cdot \boldsymbol{v} = 0 \quad \text{in } \Omega \tag{1a}$$

$$\rho\, \boldsymbol{v} \cdot \nabla \boldsymbol{v} = -\nabla p + \nabla \cdot \boldsymbol{\tau} \quad \text{in } \Omega \tag{1b}$$

$$\boldsymbol{\tau} = 2\mu(\dot{\gamma})\boldsymbol{D} \quad \text{in } \Omega \tag{1c}$$

$$\mu(\dot{\gamma}) = \mu_\infty + \frac{\mu_0 - \mu_\infty}{\left[1 + (\lambda\dot{\gamma})^a\right]^{\frac{1-n}{a}}} \quad \text{in } \Omega \tag{1d}$$

$$\dot{\gamma} = \sqrt{2\boldsymbol{D} : \boldsymbol{D}} \quad \text{in } \Omega \tag{1e}$$

$$\boldsymbol{v} = \widehat{v}_z(r)\boldsymbol{e}_z \quad \text{on } \Sigma_i \tag{1f}$$

$$\boldsymbol{v} = \boldsymbol{0} \quad \text{on } \Sigma_w \tag{1g}$$

$$v_r = 0 \wedge \tau_{rz} = 0 \quad \text{on } \Sigma_{ax} \tag{1h}$$

$$\left[(-p\boldsymbol{I} + \boldsymbol{\tau})\boldsymbol{e}_z\right] \cdot \boldsymbol{e}_z = -\widehat{p} \quad \text{on } \Sigma_o \tag{1i}$$

where $\rho$ is the bio-ink density, $\boldsymbol{\tau}$ is the symmetric second-order deviatoric stress tensor, $\boldsymbol{D}$ is the second-order strain-rate tensor defined as the symmetric part of the velocity gradient $\nabla \boldsymbol{v}$, $\mu$ is the dynamic viscosity depending on the shear rate $\dot{\gamma}$ and the five Carreau-Yasuda parameters ($\mu_0$, $\mu_\infty$, $\lambda$, $n$ and $a$), $\widehat{v}_z$ and $\widehat{p}$ are assigned inlet velocity and outlet pressure profiles, respectively.

Since the problem symmetry, the components of the strain-rate tensor $\boldsymbol{D}$ result in $D_{r\theta} = D_{\theta r} = D_{\theta z} = D_{z\theta} = 0$, and the same holds true for the counterpart components of the stress tensor $\boldsymbol{\tau}$.

With the aim to decouple extensional effects from the shear ones, it is convenient to introduce a local reference system $(\mathbf{t}, \mathbf{n})$, where $\mathbf{t}(r, z)$ and $\mathbf{n}(r, z)$ denote respectively the tangent and normal unit vectors to a bio-ink particle trajectory (see Fig. 1). Accordingly, and as detailed in [19], the shear stress ($\tau_s$) and the extensional one ($\tau_e$) result respectively in:

$$\tau_s = \tau_{nt}\,, \tag{2a}$$

$$\tau_e = \frac{\left[(\tau_{tt} - \tau_{nn})D_{tt} + (\tau_{\theta\theta} - \tau_{nn})D_{\theta\theta}\right]J_2(\boldsymbol{D})}{6\,I_3(\boldsymbol{D})}\,, \tag{2b}$$

where $J_2(\boldsymbol{D}) = \boldsymbol{D} : \boldsymbol{D}$, $I_3(\boldsymbol{D}) = \det \boldsymbol{D}$ and $\tau_{qm} = \boldsymbol{\tau} : (\mathbf{q} \otimes \mathbf{m})$ (respectively, $D_{qm} = \boldsymbol{D} : (\mathbf{q} \otimes \mathbf{m})$), with unit vectors $\mathbf{q}$ and $\mathbf{m}$ denoting $\mathbf{n}$, $\mathbf{t}$ or $\boldsymbol{e}_\theta$.

## 2.2 Cell damage model

During the extrusion process, cells can undergo mechanobiological damage. Since typical bio-inks are characterized by low cell volume fractions, damage mechanisms are essentially influenced by mechanical stresses arising from the interaction between cells and the surrounding gel matrix, while poorly affected by cell-cell interactions [26]. Generally, it is assumed that the stresses acting on cells closely resemble the local stresses experienced within the equivalent homogeneous fluid describing the bio-ink [11, 39].

The cell damage model addressed by the authors in [19] is here adopted. This model generalizes a state-of-the-art approach [26] and takes into account for:

- the shear effects in the nozzle, commonly considered as the primary cause of cell damage in bioprinting processes [26, 40–42];
- the influence of cell distribution over the nozzle cross-section, since cells are not necessarily evenly distributed when flowing in a channel [43–45];
- the extensional effects arising from the crossing of the contractive region of the extruder, since cells may suffer from extensional stresses [25, 46, 47].

Hence, the cell damage $d$ at the end of the extrusion process reads:

$$d = d(W_p^{eq}, \overline{\tau_e}) = \\ = d_{max} - \left[d_{max} - d_{e,max}\left(1 - \mathrm{e}^{-a_e \overline{\tau_e}^{b_e}}\right)\right]\mathrm{e}^{-a_p W_p^{eq}}, \quad (3)$$

where $d_{max} > 0$, $d_{e,max} \geq 0$, $a_p > 0$, $a_e > 0$ and $b_e > 0$ are model parameters, $\overline{\tau_e}$ is an average measure of extensional stresses at the nozzle inlet cross-section (i.e., at $z = L_c$, Fig. 1) and $W_p^{eq}$ is the equivalent pressure work, that is an energy measure that gathers physical parameters that may affect shear stress distribution on cells. In particular, it is computed as:

$$W_p^{eq} = \frac{1}{2}\Delta p_n A_{eq} L_n, \quad (4)$$

where $\Delta p_n$ denotes the total pressure drop in the nozzle and $A_{eq} \leq A$ identifies a measure of the area portion of the nozzle cross-section interested by cell distribution described as:

$$A_{eq}(A) := \begin{cases} A\mathrm{e}^{-k_1 A} & \text{if } 0 < A \leq A_0 \\ A_{eq,0} + \frac{(A_{eq,\infty} - A_{eq,0})}{\left[1 - \mathrm{e}^{-k_2\left(A - A_0\right)}\right]^{-1}} & \text{if } A > A_0 \end{cases}, \quad (5)$$

$A$ being the nozzle cross-section, $A_0 > 0$, $A_{eq,\infty} > 0$, $k_1 \geq 0$ and $k_2 \geq 0$ being model parameters and $A_{eq,0} = A_0 \mathrm{e}^{-k_1 A_0}$.

Finally, cell viability $c_v$ at the end of the extrusion process can be assessed as:

$$c_v(W_p^{eq}, \overline{\tau_e}) = 1 - d(W_p^{eq}, \overline{\tau_e}). \quad (6)$$

### 2.3 High-fidelity CFD simulations

The steady-state differential problem introduced in Sect. 2.1 is faced via a Finite Element formulation, detailed in [19] and that allows to obtain a high-fidelity description of the bio-ink response. Computational-fluid-dynamics (CFD) simulations have been carried out by using a mixed Galerkin formulation implemented through the AceGen package of Wolfram Mathematica [48, 49]. The computational domain describing the extruder geometry is discretized via axisymmetric Taylor-Hood $P_2P_1$ triangular elements in the $(r, z)$ plane such that velocity and pressure fields are interpolated via quadratic and linear lagrangian shape functions, respectively. Specifically, numerical CFD solutions are employed to compute the following quantities:

- the pressure drop $\Delta p_c$ in the contractive region of the extruder, that is for $0 \leq z \leq L_c$;
- the average extensional stress $\overline{\tau_e}$ at the nozzle inlet cross-section computed as:

$$\overline{\tau_e} = \frac{4}{\pi D^2}\int_0^{D/2} \tau_e\big|_{z=L_c} 2\pi r\, dr, \quad (7)$$

  where $D$ is the nozzle diameter;
- the pressure drop per unit length $\Delta p_n / L_n$ in the nozzle, that is for $L_c \leq z \leq L_c + L_n$.

In bioprinting applications a laminar flow regime can be considered, since the expected Reynolds numbers are in the range $10^{-5} \div 10^{-1}$ (the bio-ink density $\rho$, the extrusion velocity $\overline{v}$, the nozzle diameter $D$ and the bio-ink dynamic viscosity $\mu$ are in the order of $10^3$ kg/m$^3$, $10^{-2}$ m/s, $10^{-4}$ m and $10^{-2} \div 10^2$ Pa·s, respectively). Hence, a fully-developed state is expected within the nozzle not so far from the contractive region and a reduced length $L_n' < L_n$ can be considered for the nozzle domain to minimize the computational workload. Therefore, the pressure drop per unit length $\Delta p_n / L_n$ in the nozzle can be estimated from the CFD results as:

$$\frac{\Delta p_n}{L_n} \simeq \frac{p|_{z=L_c} - p|_{z=L_c+L_n'}}{L_n'}. \quad (8)$$

Consistently with the differential problem introduced in Sect. 2.1, the following boundary conditions are enforced (see notation in Fig. 1):

- the velocity profile at the inlet section (i.e., at $z = 0$) is defined by using the velocity profile of

a reference Newtonian-Poiseuille flow, that is by prescribing $\hat{v}_z = 2\left[\overline{v}(D/D_{in})^2\right]\left[1-(2r/D_{in})^2\right]$, where $\overline{v}$ is the mean outflow velocity and $D_{in}$ is the inlet extruder diameter;
- the pressure profile at the computational outflow boundary (i.e., at $z = L_c + L_n'$) is prescribed as uniform and equal to zero, as a reference value.

The rationale behind setting a Newtonian velocity profile at the inlet boundary is grounded in the combination of low mean inflow velocity (in the order of $10^{-4}$ m/s) and a large inlet radius (in the order of $10^{-3}$ m), resulting in notably low shear rates (in the order of $10^{-1}$ $s^{-1}$). As a result, in the proximity of the inlet region, the rheology of the fluid is described by the low shear rate plateu of the flow curve exhibiting a Newtonian behaviour with a dynamic viscosity equivalent to $\mu_0$.

### 2.4 Reduced-order model and nomograms

The outcomes obtained from CFD simulations are used to build a reduced-order model (ROM) capable of summarizing the interconnections among fundamental process variables. By applying the Buckingham $\pi$ Theorem and by adopting arguments of dimensional analysis [50], the following relationships can be obtained for the assessment of the post-processing quantities of interest:

$$\Delta p_c(D,\overline{v}) = \frac{\overline{\mu}\,\overline{v}}{D}\frac{\alpha_{c,1}\left(\frac{D}{D_{in}}\right)^{\alpha_{c,2}}+\alpha_{c,3}}{\left(\frac{\rho\overline{v}D}{\overline{\mu}}\right)^{\beta_{c,1}\left(\frac{D}{D_{in}}\right)^{\beta_{c,2}}+\beta_{c,3}}}, \tag{9a}$$

$$\overline{\tau_e}(D,\overline{v}) = \frac{\overline{\mu}\,\overline{v}}{D}\frac{\alpha_{e,1}\left(\frac{D}{D_{in}}\right)^{\alpha_{e,2}}+\alpha_{e,3}}{\left(\frac{\rho\overline{v}D}{\overline{\mu}}\right)^{\beta_{e,1}\left(\frac{D}{D_{in}}\right)^{\beta_{e,2}}+\beta_{e,3}}}, \tag{9b}$$

$$\frac{\Delta p_n}{L_n}(D,\overline{v}) = \frac{\overline{\mu}\,\overline{v}}{D^2}\frac{\alpha_{n,1}\left(\frac{D}{L_n}\right)^{\alpha_{n,2}}+\alpha_{n,3}}{\left(\frac{\rho\overline{v}D}{\overline{\mu}}\right)^{\beta_{n,1}\left(\frac{D}{L_n}\right)^{\beta_{n,2}}+\beta_{n,3}}}, \tag{9c}$$

where $\alpha_{y,i}$ and $\beta_{y,i}$ (with $y = c, e, n$ and $i = 1, 2, 3$) are model parameters tuned through the 2-step calibration procedure detailed in [19] and $\overline{\mu} = (\mu_0 + \mu_\infty)/2$ is an average measure of the dynamic viscosity.

The calibration of such a reduced-order model enables the construction of specific bio-ink nomograms, that is diagrams that straight furnish a visual representation summarizing the non-linear relationships among five key interrelated process variables:

- the nozzle diameter $D$ and the extrusion velocity $\overline{v}$ (process input);
- the printing pressure $\Delta p$ evaluated as $\Delta p_c + \Delta p_n$ with $\Delta p_c$ and $\Delta p_n$ determined from Eqs. (9a) and (9c), the mass flow rate $\dot{m}$ and the cell viability $c_v$ (process output).

Nomograms are here built in the plane of $(D, \overline{v})$, where the relationship with the mass flow rate $\dot{m}$ is highlighted by isopleths at constant values of $\dot{m}$, and where the correponding values of the printing pressure $\Delta p$ and cell viability $c_v$ are depicted through colormap representations.

## 3 Results and discussion

The in silico approach proposed in [19] is here applied by referring to the following scenarios:

- Three different shapes of the cartridge-nozzle connection region are addressed. Two of them (Fig. 2a and b) are characterized by an abrupt cross-section reduction (inspired by [25] and [15]). The last one is featured with a smooth cross-section reduction characterized by a parabolic profile (Fig. 2c). The extruder geometrical parameters adopted for the analyzed case studies are reported in Table 1. Moreover, in agreement with commercially-available devices [51], the nozzle diameter $D$ is considered in the range $0.15 \div 0.51$ mm;
- Two different bio-ink polymer types, namely a 3 wt% alginate solution (in the following referred to as bio-ink 1) and a 6 wt% chitosan solution (bio-ink 2). Figure 3 depicts the rheological behaviour of both bio-inks described through the adopted Carreau-Yasuda model. Table 2 summarizes the corresponding rheological parameters (see [19] for bio-ink 1, [52] for bio-ink 2), together with polymer weigth concentrations and mass densities.

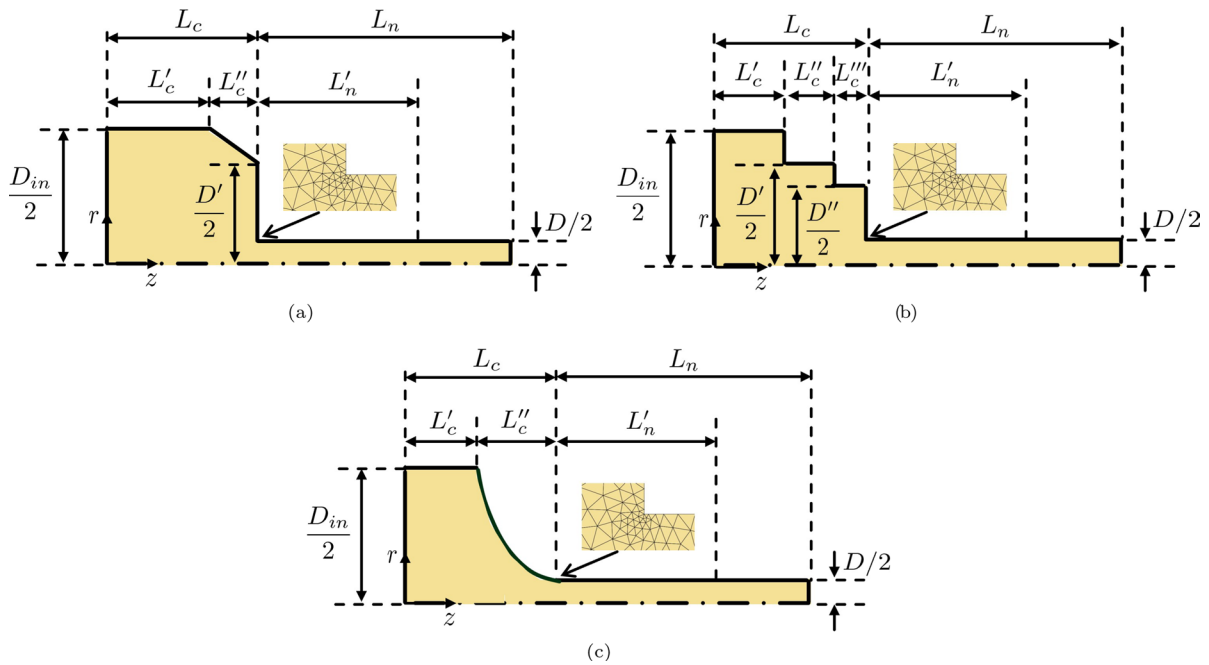


**Fig. 2** Geometrical details of the three axisymmetric extruders considered for numerical applications: **a** extruder 1; **b** extruder 2; **c** extruder 3

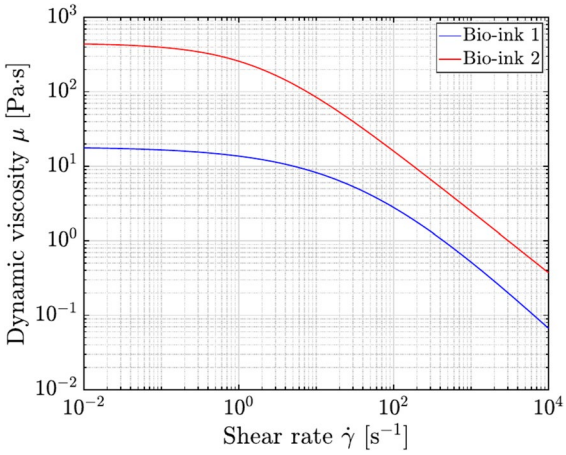


**Fig. 3** Dynamic viscosity $\mu$ vs. shear rate $\dot{\gamma}$ for the bio-inks analiyzed in the present study

Numerical solutions are obtained by considering a domain discretization (refined at the cartridge-nozzle connection where the highest gradients are expected) consisting in about 39000÷53000 elements, as a result of a preliminary convergence analysis. In addition, different values of the extrusion velocity $\bar{v}$ have been analyzed within the common range of interest for extrusion-based bioprinting processes (6÷24 mm/s, in agreement with [41]).

### 3.1 CFD simulations

In this section, exemplary results obtained via high-fidelity CFD simulations are presented and analyzed. In particular, for the sake of compactness, only the case study with $D = 0.33$ mm and $\bar{v} = 15$ mm/s is

**Table 1** Geometrical parameters adopted for defining the extruder models (see Fig. 2)

| Extruder | $D$ (mm) | $D_{in}$ (mm) | $D'$ (mm) | $D''$ (mm) | $L_n$ (mm) | $L'_n = L_c$ (mm) | $L'_c$ (mm) | $L''_c$ (mm) | $L'''_c$ (mm) |
|---|---|---|---|---|---|---|---|---|---|
| 1 | 0.15÷0.51 | 2.64 | 2.00 | – | 11.9 | 1.50 | 1.00 | 0.50 | – |
| 2 | 0.15÷0.51 | 2.64 | 2.00 | 1.60 | 11.9 | 1.50 | 0.70 | 0.50 | 0.30 |
| 3 | 0.15÷0.51 | 2.64 | – | – | 11.9 | 1.50 | 0.70 | 0.80 | – |

**Table 2** Material properties for the bio-inks analyzed in the present study (see [19] for rheological parameters of bio-ink 1, [52] for bio-ink 2)

| Bio-ink | Polymer type | wt (%) | $\rho$ (kg/m$^3$) | $\mu_0$ ( Pa·s) | $\mu_\infty$ ( Pa·s) | $\lambda$ (s) | $n$ (–) | $a$ (–) |
|---|---|---|---|---|---|---|---|---|
| 1 | Alginate | 3 | 1000 | 18.190 | 0.001 | 0.02453 | 0 | 0.5035 |
| 2 | Chitosan | 6 | 1000 | 452.000 | 0.001 | 0.520 | 0.170 | 0.720 |

discussed for all the extruder geometries and the bio-inks analyzed. Figures 4, 5, 6 show extensional and shear stress fields within the extruder, as well as trajectory and stress measures numerically experienced by a bio-ink particle moving from an inlet radial position identified at 60% of the inlet radius. A comparative analysis of case studies associated with extruder 1 and extruder 2 depicts sligth differences in both stress field for the same bio-ink but different extruder geometry. On the other hand, remarkable differences in the extensional stress field occur when the extruder geometry 3 is adopted. In detail, a more homogeneous distribution of the extensional stresses along the cartridge-nozzle connection region and lower peaks and average values of the extensional stresses (3÷4 times) are observed for extruder 3.

Instead, both stress fields result very different when the bio-ink varies at fixed extruder geometry. The higher viscosity of bio-ink 2 (see Fig. 3) leads to stresses resulting an order of magnitude higher than

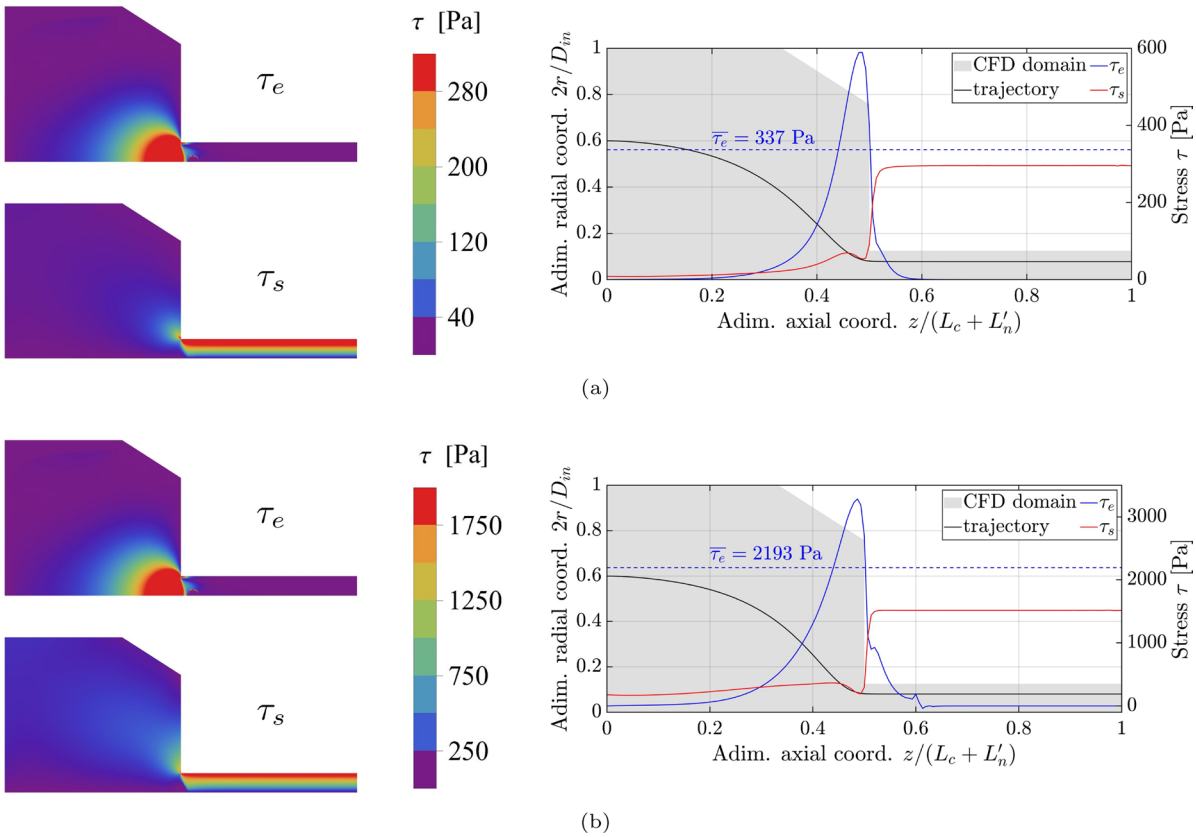


**Fig. 4** Contour plots of extensional stress $\tau_e$ [Pa] (on the top left) and shear stress $\tau_s$ [Pa] (on the bottom left); trajectory and stresses experienced by a bio-ink particle moving from an inlet radial position identified at 60% of the inlet radius (on the right). Case studies with extruder 1, $D = 0.33$ mm and $\overline{v} = 15$ mm/s for: **a** bio-ink 1; **b** bio-ink 2

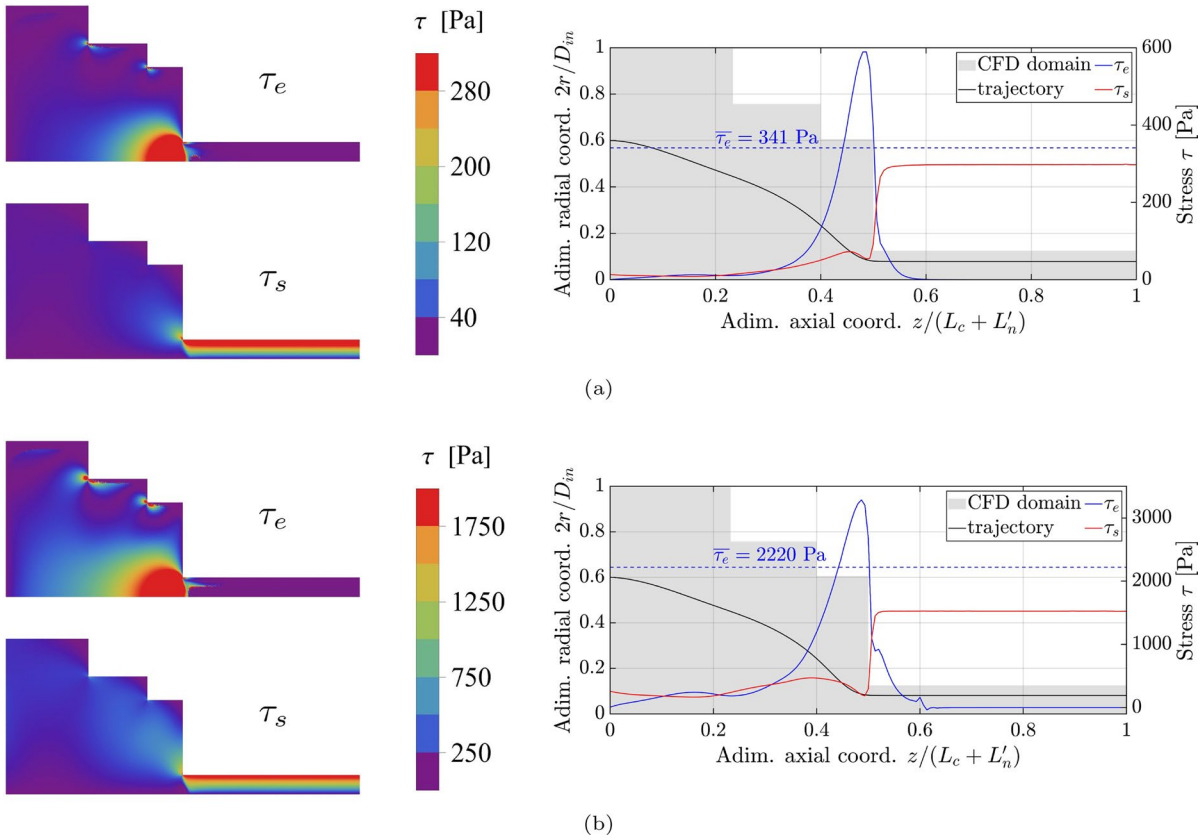


**Fig. 5** Contour plots of extensional stress $\tau_e$ [Pa] (on the top left) and shear stress $\tau_s$ [Pa] (on the bottom left); trajectory and stresses experienced by a bio-ink particle moving from an inlet radial position identified at 60% of the inlet radius (on the right). Case studies with extruder 2, $D = 0.33$ mm and $\overline{v} = 15$ mm/s for: **a** bio-ink 1; **b** bio-ink 2

the case of bio-ink 1. Moreover, results allow to quantify the region where extensional stresses are dominant with respect to shear stresses as function of the cartridge-nozzle geometry.

### 3.2 Calibration and validation of the reduced-order model

The model parameters $\alpha_{y,i}$ and $\beta_{y,i}$ (with $y = c, e, n$ and $i = 1, 2, 3$) defining the reduced-order model (ROM) relationships introduced in Sect. 2.4 have been calibrated on the basis of 35 high-fidelity CFD simulations (for each extruder geometry and bio-ink type). In detail, 5 values of the nozzle diameter $D$ (i.e., 0.15, 0.25, 0.33, 0.41 and 0.51 mm) and 7 values of the extrusion velocity $\overline{v}$ (i.e., 6, 9, 12, 15, 18, 21 and 24 mm/s) are considered. Moreover, 30 additional simulations are performed to validate the ROM predictions, by setting 5 different values for $D$ (0.20, 0.30, 0.35, 0.45 and 0.55 mm) and 6 for $\overline{v}$ (7.5, 10.5, 13.5, 16.5, 19.5 and 22.5 mm/s).

High-fidelity values of post-processing quantities in Eqs. (9) are compared with ROM values on the full datasets (the union of calibration and validation datasets). In Table 3 the calibrated parameters of the ROM model and the final mean relative errors are reported for all the analyzed case studies. The obtained values prove the excellent performance of the proposed approach.

### 3.3 Nomograms

The complex non-linear relationships among process variables are highlighted and quantified through nomograms proposed in Fig. 7 (for extruder 1) and Fig. 8 (for extruder 3). In detail, Figs. 7a and 8a

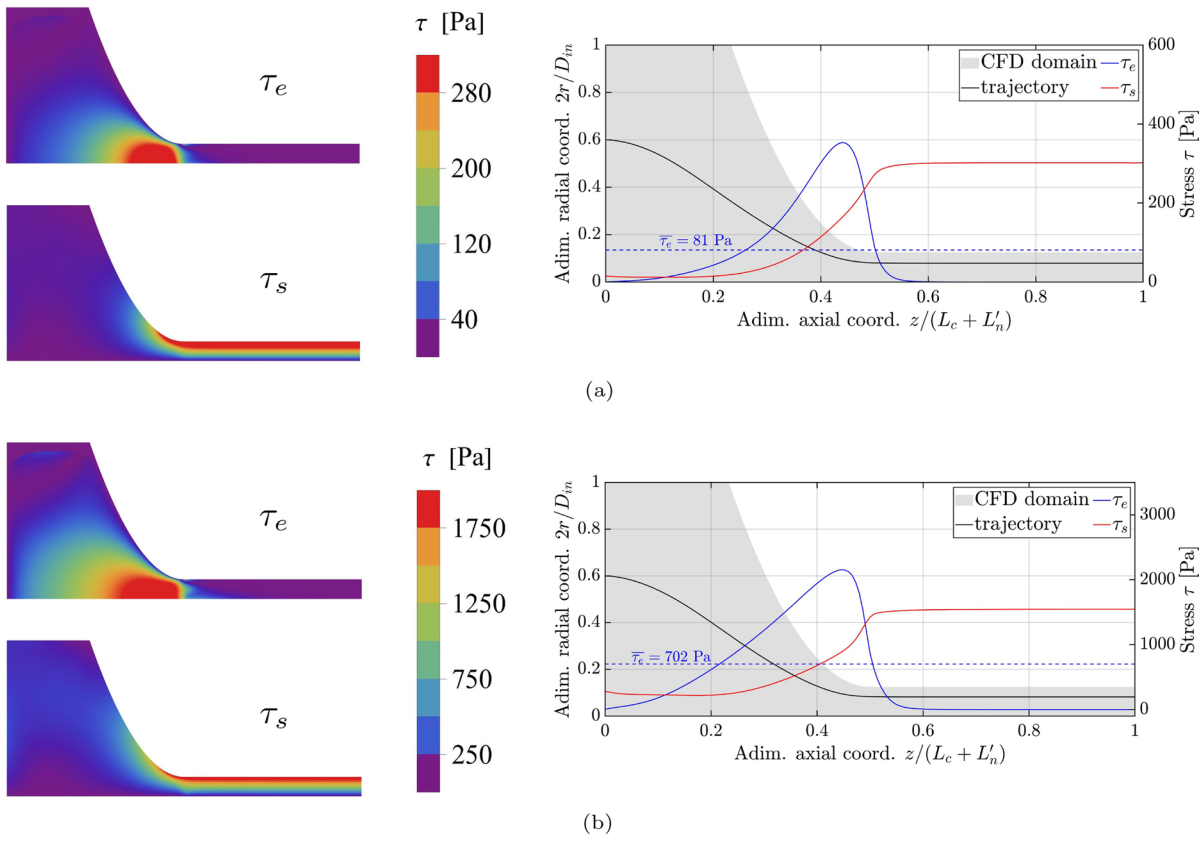


**Fig. 6** Contour plots of extensional stress $\tau_e$ [Pa] (on the top left) and shear stress $\tau_s$ [Pa] (on the bottom left); trajectory and stresses experienced by a bio-ink particle moving from an inlet radial position identified at 60% of the inlet radius (on the right). Case studies with extruder 3, $D = 0.33$ mm and $\overline{v} = 15$ mm/s for: **a** bio-ink 1; **b** bio-ink 2

(respectively, Figs. 7b and 8b) show, in the parameter space of nozzle diameter $D$ and extrusion velocity $\overline{v}$, the colormaps of printing pressure $\Delta p$ and cell viability $c_v$, as well as the isopleths of mass flow rate $\dot{m}$ for the case study with bio-ink 1 (resp., bio-ink 2). For the assessment of the cell viability, the damage law described in Sect. 2.2 is adopted, by assuming as model parameters the values reported in [19]. For the sake of compactness, nomograms for extruder 2 are not reported since the slight differences in terms of printing pressure and cell viability with respect to the case study with extruder 1.

By addressing the same bio-ink but different extruder geometries (cf., Figs. 7a and 8a or Figs. 7b and 8b), minor differences in printing pressure are obtained. On the other hand, more relevant differences in cell viability can be noted. In detail, higher cell viabilities are numerically experienced for the case studies associated with extruder 3, especially for the lowest values of nozzle diameter, thanks to the lower values of extensional stresses obtained with a smooth parabolic connection between cartridge and nozzle (cf., Figs. 4 and 6).

Instead, when referring to different bio-inks and the same extruder geometry (cf., Fig. 7a and b or Fig. 8a and b), very different values of both printing pressure and cell viability are obtained. Specifically, for bio-ink 2 the printing pressure, as well as shear and extensional stresses, are an order of magnitude higher than bio-ink 1 since bio-ink 2 is more visocus across the entire range of shear-rates considered. This results in lower cell viability than the case associated with bio-ink 1. As a matter of fact, the best performances in terms of cell viability for bio-ink 2 (associated with low values of nozzle diameter and extrusion velocity) are comparable with the worst performances for bio-ink 1 (associated with high values of nozzle diameter and extrusion velocity).

**Table 3** Values of model parameters defining the proposed reduced-order model and final mean relative errors obtained from the comparison between high-fidelity values of post-processing quantities in Eqs. (9) and ROM values on the full datasets (the union of calibration and validation datasets)

| | Model parameters | | | | | | |
|---|---|---|---|---|---|---|---|
| | $\alpha_{y,1}$ | $\alpha_{y,2}$ | $\alpha_{y,3}$ | $\beta_{y,1}$ | $\beta_{y,2}$ | $\beta_{y,3}$ | $\overline{\text{err}}$ |
| *Extruder 1 and Bio-ink 1* | | | | | | | |
| $\Delta p_c$ | 1.2420 | 1.6089 | − 0.0025 | − 1.2992 | 0.0771 | 1.6567 | 0.84 % |
| $\overline{\tau_e}$ | 0.9413 | 1.9830 | 0.0001 | − 0.6639 | 0.4812 | 0.7738 | 1.29 % |
| $\frac{\Delta p_n}{L_n}$ | 78.9450 | 2.2621 | − 0.0005 | − 1.1435 | 0.2254 | 1.2156 | 1.07 % |
| *Extruder 1 and Bio-ink 2* | | | | | | | |
| $\Delta p_c$ | 0.0100 | 1.4010 | $-5 \cdot 10^{-5}$ | 0.0170 | − 0.4946 | 0.6327 | 0.73 % |
| $\overline{\tau_e}$ | 0.0100 | 2.2920 | $4 \cdot 10^{-6}$ | − 0.3988 | 0.7825 | 0.8061 | 1.27 % |
| $\frac{\Delta p_n}{L_n}$ | 0.2050 | 1.9800 | $7 \cdot 10^{-6}$ | − 0.4751 | 0.7824 | 0.8292 | 0.51 % |
| *Extruder 2 and Bio-ink 1* | | | | | | | |
| $\Delta p_c$ | 1.3430 | 1.6440 | − 0.0024 | − 1.0893 | 0.0983 | 1.4366 | 0.83 % |
| $\overline{\tau_e}$ | 0.8819 | 1.9420 | $4 \cdot 10^{-7}$ | − 0.7265 | 0.3226 | 0.8960 | 2.03 % |
| $\frac{\Delta p_n}{L_n}$ | 79.2500 | 2.2640 | − 0.0005 | − 0.7265 | 0.3236 | 0.8960 | 1.03 % |
| *Extruder 2 andBio-ink 2* | | | | | | | |
| $\Delta p_c$ | 0.0099 | 1.3910 | $-5 \cdot 10^{-5}$ | 0.0040 | − 0.8500 | 0.6554 | 1.07 % |
| $\overline{\tau_e}$ | 0.0083 | 2.2080 | $6 \cdot 10^{-6}$ | − 0.3368 | 0.5958 | 0.8243 | 2.00 % |
| $\frac{\Delta p_n}{L_n}$ | 0.2173 | 2.0000 | $9 \cdot 10^{-6}$ | − 0.4742 | 0.7830 | 0.8291 | 0.73 % |
| *Extruder 3 and Bio-ink 1* | | | | | | | |
| $\Delta p_c$ | 1.0892 | 1.3637 | − 0.0068 | 0.8494 | − 0.0875 | − 0.4372 | 0.96 % |
| $\overline{\tau_e}$ | 0.1153 | 1.2726 | − 0.0006 | $2 \cdot 10^{-5}$ | − 2.1863 | 0.4293 | 1.16 % |
| $\frac{\Delta p_n}{L_n}$ | 75.1173 | 2.2613 | − 0.0004 | − 1.1252 | 0.2369 | 1.1912 | 1.06 % |
| *Extruder 3 and Bio-ink 2* | | | | | | | |
| $\Delta p_c$ | 0.0066 | 1.3480 | $4 \cdot 10^{-5}$ | 0.0001 | − 1.8252 | 0.7258 | 3.41 % |
| $\overline{\tau_e}$ | 0.0056 | 1.9770 | $-6 \cdot 10^{-6}$ | 0.0779 | − 0.3220 | 0.4710 | 0.98 % |
| $\frac{\Delta p_n}{L_n}$ | 0.2209 | 2.0000 | $6 \cdot 10^{-6}$ | − 0.7953 | 0.9397 | 0.8274 | 0.54 % |

## 4 Conclusions

In the realm of bioprinting planning, establishing suitable settings for fundamental process variables (such as printing pressure, nozzle diameter, target extrusion velocity, mass flow rate, and desired cell viability) can be challenging, thus leading to expensive trial-and-error routines for protocols definition.

By adopting the in silico approach recently proposed by the authors [19], the present study aims to apply the proposed methodological approach with different bio-inks and different geometries of the extrusion system, showing how it enables a reasoned and swift establishment of suitable target conditions. Thus, the proposed modeling strategy paves the way to reduce the time-consuming and expensive trial-and-error experimental procedures actually performed in laboratory practice.

The analyzed case studies confirm that the developed tool gives quantitative information on the effect of the choice of the bio-ink polymer type. For instance, the chitosan-based bio-ink (bio-ink 2) is associated with higher printing pressure with respect to the alginate-based one at the same nozzle diameter and extrusion velocity. The proposed strategy allows to translate this outcome, well known in the laboratory practice, in quantitative terms and towards a more informed decision making process. In fact, the developed nomograms allow to identify regions in the process setting space where the two bio-inks can be extruded with similar printing pressures. In addition, in silico results provide values of the extensional stresses that are attained in the cartridge-nozzle connection region, together with more standard shear stresses in the nozzle. A cell damage law is then applied to build informative nomograms

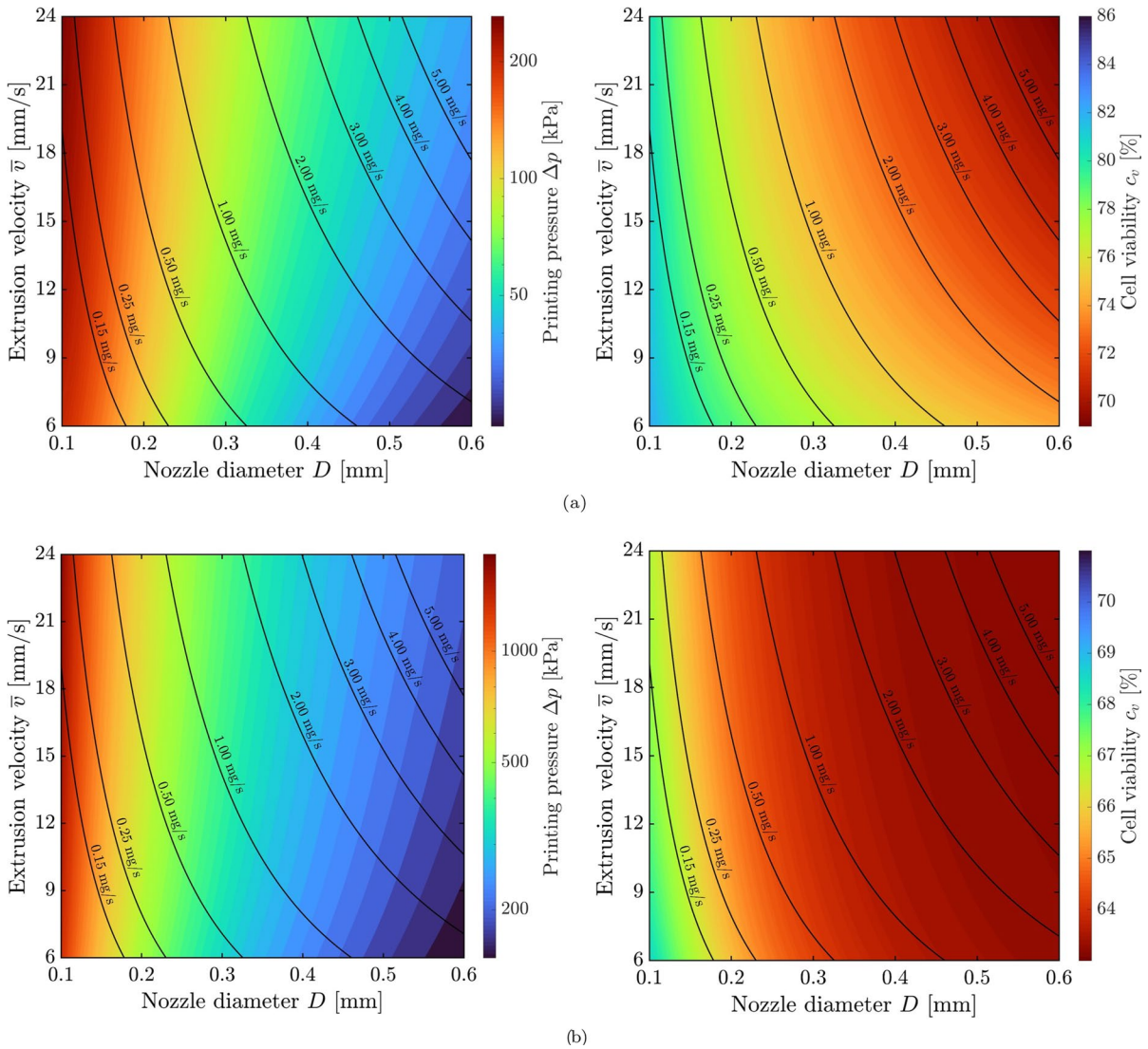


**Fig. 7** Nomograms built from the reduced-order model for the case studies associated with extruder 1: colormap of printing pressure and mass flow rate isopleths (on the left); colormap of cell viability and mass flow rate isopleths (on the right). **a** Case study with bio-ink 1; **b** case study with bio-ink 2. Cell damage model parameters adopted [19]: $A_0 = 0.50$ mm$^2$, $A_{eq,\infty} = 0.70$ mm$^2$, $k_1 = 0$ mm$^{-2}$, $k_2 = 4$ mm$^{-2}$, $b_e = 0.3654$, $a_e = 0.1752$ Pa$^{-b_e}$, $a_p = 0.0211$ $\mu$J$^{-1}$, $d_{e,max} = 0.1725$ and $d_{max} = 0.3681$

of cell viability for the two bio-inks, confirming how the higher pressure required for chitosan-based bio-ink translate into higher risk of cell damage during the extrusion process. Furthermore, the design of the cartridge-nozzle connection also appears to play an important role. Indeed, an *ad-hoc* design of the extruder might be useful to minimize the extensional stresses arising around the cartridge-nozzle connection region, as it follows from computational results associated with extruder 3.

Clearly, our work is not yet exempt from limitations. The proposed modeling strategy should be verified towards more and more bio-ink types (differing in cell types, cell densities and/or polymer types) and geometries of the extrusion system. The study could be also enhanced in order to describe the viscoelastic flow of the bio-ink outside of the nozzle, allowing to possibly account for loss of printing resolution and some post-printing mechanisms ([53], [54]).

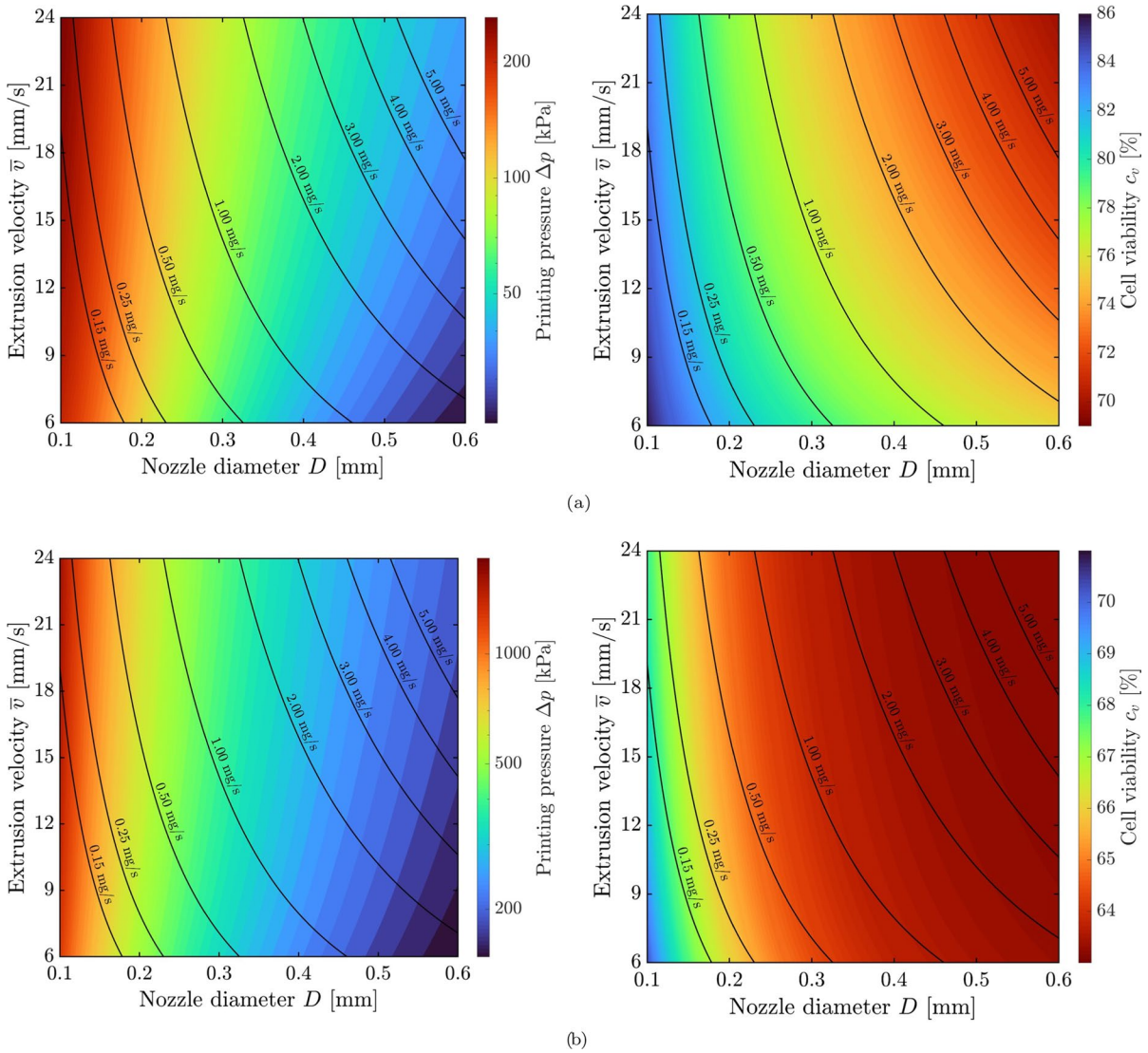


**Fig. 8** Nomograms built from the reduced-order model for the case studies associated with extruder 3: colormap of printing pressure and mass flow rate isopleths (on the left); colormap of cell viability and mass flow rate isopleths (on the right). **a** Case study with bio-ink 1; **b** case study with bio-ink 2. Cell damage model parameters adopted [19]: $A_0 = 0.50$ mm$^2$, $A_{eq,\infty} = 0.70$ mm$^2$, $k_1 = 0$ mm$^{-2}$, $k_2 = 4$ mm$^{-2}$, $b_e = 0.3654$, $a_e = 0.1752$ Pa$^{-b_e}$, $a_p = 0.0211$ $\mu$J$^{-1}$, $d_{e,max} = 0.1725$ and $d_{max} = 0.3681$

**Acknowledgements** This work is partially funded by Regione Lazio (POR FESR LAZIO 2014-2020; Progetti di Gruppi di Ricerca 2020; project: BIOPMEAT, n. A0375-2020-36756). Part of this work was carried out with the support from the Italian National Group for Mathematical Physics (GNFM-INdAM).

**Funding** Open access funding provided by Università degli Studi di Roma Tor Vergata within the CRUI-CARE Agreement. This work is partially funded by Regione Lazio (POR FESR LAZIO 2014-2020; Progetti di Gruppi di Ricerca 2020; project: BIOPMEAT, n. A0375-2020-36756). Part of this work was carried out with the support from the Italian National Group for Mathematical Physics (GNFM-INdAM).

**Availability of data and materials** Data will be made available on request.

**Declarations**

**Conflict of interest** The authors declare that they have no Conflict of interest.

**Ethical approval** Not applicable.

## References

1. Murphy S, Atala A (2014) 3d bioprinting of tissues and organs. Nat Biotechnol 32:773–785. https://doi.org/10.1038/nbt.2958
2. Ozbolat IT, Hospodiuk M (2016) Current advances and future perspectives in extrusion-based bioprinting. Biomaterials 76:321–343. https://doi.org/10.1016/j.biomaterials.2015.10.076
3. Cadamuro F, Marongiu L, Marino M, Tamini N, Nespoli L, Zucchini N, Terzi A, Altamura D, Gao Z, Giannini C, Bindi G, Smith A, Magni F, Bertini S, Granucci F, Nicotra F, Russo L (2023) 3d bioprinted colorectal cancer models based on hyaluronic acid and signalling glycans. Carbohydr Polym 302:120395. https://doi.org/10.1016/j.carbpol.2022.120395
4. Bari E, Di Gravina GM, Scocozza F, Perteghella S, Frongia B, Tengattini S, Segale L, Torre ML, Conti M (2023) Silk fibroin bioink for 3d printing in tissue regeneration: controlled release of msc extracellular vesicles. Pharmaceutics 15:383. https://doi.org/10.3390/pharmaceutics15020383
5. Chiesa I, Maria CD, Lapomarda A, Fortunato GM, Montemurro F, Gesù RD, Tuan RS, Vozzi G, Gottardi R (2020) Endothelial cells support osteogenesis in an in vitro vascularized bone model developed by 3d bioprinting. Biofabrication 12:025013. https://doi.org/10.1088/1758-5090/ab6a1d
6. Fornetti E, Paolis FD, Fuoco C, Bernardini S, Giannitelli SM, Rainer A, Seliktar D, Magdinier F, Baldi J, Biagini R, Cannata S, Testa S, Gargioli C (2023) A novel extrusion-based 3d bioprinting system for skeletal muscle tissue engineering. Biofabrication 15:025009. https://doi.org/10.1088/1758-5090/acb573
7. Zhang YS, Haghiashtiani G, Hübscher T, Kelly D, Lee JM, Lutolf M, McAlpine M, Yeong WY, Zenobi M, Malda J (2021) 3d extrusion bioprinting. Nat Rev Dis Prim 1:75. https://doi.org/10.1038/s43586-021-00073-8
8. Cui X, Li J, Hartanto Y, Durham M, Tang J, Zhang H, Hooper G, Lim K, Woodfield T (2020) Advances in extrusion 3d bioprinting: a focus on multicomponent hydrogel-based bioinks. Adv Healthc Mater 9:1901648. https://doi.org/10.1002/adhm.201901648
9. Monaldo E, Hille HC, De Lorenzis L (2023) Modelling of extrusion-based bioprinting via floating isogeometric analysis (fliga). In: Fuschi P, Pisano AA (eds) Book of abstracts GIMC GMA GBMA 2023, pp 84–85. Edizioni Centro Stampa di Ateneo—Università degli Studi di Reggio Calabria "Mediterranea", Reggio Calabria (Italy) . isbn:978-88-99352-95-0. https://gimc-gma-gbma.aimeta.it/files/rc/book_of_abstracts.pdf
10. Hospodiuk M, Dey M, Sosnoski DM, Ozbolat IT (2017) The bioink: a comprehensive review on bioprintable materials. Biotechnol Adv 35:217–239. https://doi.org/10.1016/j.biotechadv.2016.12.006
11. Boularaoui S, Hussein G, Khan K, Christoforou N, Stefanini C (2020) An overview of extrusion-based bioprinting with a focus on induced shear stress and its effect on cell viability. Bioprinting 20:00093. https://doi.org/10.1016/j.bprint.2020.e00093
12. Sun W, Starly B, Daly AC, Burdick JA, Groll J, Skeldon G, Shu W, Sakai Y, Shinohara M, Nishikawa M, Jang J, Cho D-W, Nie M, Takeuchi S, Ostrovidov S, Khademhosseini A, Kamm RD, Mironov V, Moroni L, Ozbolat IT (2020) The bioprinting roadmap. Biofabrication 12:022002. https://doi.org/10.1088/1758-5090/ab5158
13. Reina-Romo E, Mandal S, Amorim P, Bloemen V, Ferraris E, Geris L (2021) Towards the experimentally-informed in silico nozzle design optimization for extrusion-based bioprinting of shear-thinning hydrogels. Front Bioeng Biotechnol 9:701778. https://doi.org/10.3389/fbioe.2021.701778
14. Moroni L, Boland T, Burdick JA, De Maria C, Derby B, Forgacs G, Groll J, Li Q, Malda J, Mironov VA, Mota C, Nakamura M, Shu W, Takeuchi S, Woodfield TBF, Xu T, Yoo JJ, Vozzi G (2018) Biofabrication: a guide to technology and terminology. Trends Biotechnol 36:384–402. https://doi.org/10.1016/j.tibtech.2017.10.015
15. Bonatti AF, Chiesa I, Vozzi G, De Maria C (2021) Open-source cad-cam simulator of the extrusion-based bioprinting process. Bioprinting 24:00172. https://doi.org/10.1016/j.bprint.2021.e00172
16. Dababneh A, Ozbolat I (2014) Bioprinting technology: a current state-of-the-art review. ASME J Manuf Sci Eng 136:061016. https://doi.org/10.1115/1.4028512
17. Loi G, Stucchi G, Scocozza F, Cansolino L, Cadamuro F, Delgrosso E, Riva F, Ferrari C, Russo L, Conti M (2023) Characterization of a bioink combining extracellular matrix-like hydrogel with osteosarcoma cells: preliminary results. Gels 9:129. https://doi.org/10.3390/gels9020129
18. Daly AC, Prendergast ME, Hughes AJ, Burdick JA (2021) Bioprinting for the biologist. Cell 184:18–32. https://doi.org/10.1016/j.cell.2020.12.002
19. Chirianni F, Vairo G, Marino M (2024) Development of process design tools for extrusion-based bioprinting: from numerical simulations to nomograms through reduced-order modeling. Comput Methods Appl Mech Eng 419:116685. https://doi.org/10.1016/j.cma.2023.116685
20. Chirianni F, Vairo G, Marino M (2023) An in-silico approach for process design in extrusion-based bioprinting. In: Fuschi P, Pisano AA (eds) Book of Abstracts GIMC GMA GBMA 2023, pp 114–115. Edizioni Centro Stampa di Ateneo—Università degli Studi di

Reggio Calabria "Mediterranea", Reggio Calabria (Italy). isbn:978-88-99352-95-0. https://gimc-gma-gbma.aimeta.it/files/rc/book_of_abstracts.pdf
21. Chirianni F, Vairo G, Marino M (2023) Process design in extrusion-based bioprinting. In: Ramos A, Furtado C, Colaço A, Arteiro A, Furtado A, Horas C, Lopes I, Carvalho R, Pereira S (eds) Proceedings of the 7th ECCOMAS Young Investigators Conference (ECCOMAS YIC 2023), pp 191–192. Zenodo, Porto (Portugal). https://doi.org/10.5281/zenodo.8393048
22. Emmermacher J, Spura D, Cziommer J, Kilian D, Wollborn T, Fritsching U, Steingroewer J, Walther T, Gelinsky M, Lode A (2020) Engineering considerations on extrusion-based bioprinting: interactions of material behavior, mechanical forces and cells in the printing needle. Biofabrication 12:025022. https://doi.org/10.1088/1758-5090/ab7553
23. Müller S, Mirzahossein E, Iftekhar E, Bächer C, Schrüfer S, Schubert D, Fabry B, Gekle S (2020) Flow and hydrodynamic shear stress inside a printing needle during biofabrication. PLoS One 15:0236371. https://doi.org/10.1371/journal.pone.0236371
24. Tian XY, Li MG, Chen XB (2013) Bio-rapid-prototyping of tissue engineering scaffolds and the process-induced cell damage. J Biomim Biomater Biomed Eng 17:1–23. https://doi.org/10.4028/www.scientific.net/JBBTE.17.1
25. Ning L, Betancourt N, Schreyer DJ, Chen X (2018) Characterization of cell damage and proliferative ability during and after bioprinting. ACS Biomater Sci Eng 4:3906–18. https://doi.org/10.1021/acsbiomaterials.8b00714
26. Han S, Kim CM, Jin S, Kim TY (2021) Study of the process-induced cell damage in forced extrusion bioprinting. Biofabrication 13:035048. https://doi.org/10.1088/1758-5090/ac0415
27. Li M, Tian X, Zhu N, Schreyer D, Chen X (2009) Modeling process-induced cell damage in the biodispensing process. Tissue Eng C 16:533–42. https://doi.org/10.1089/ten.TEC.2009.0178
28. Ning L, Yang B, Mohabatpour F, Betancourt N, Sarker M, Papagerakis P, Chen D (2019) Process-induced cell damage: pneumatic vs. screw-driven bioprinting. Biofabrication 12:025011. https://doi.org/10.1088/1758-5090/ab5f53
29. Yang J, Dai Y, Li J (2014) A different extensional viscosity prediction based on entry pressure drop. J Appl Polym Sci 131:40563. https://doi.org/10.1002/app.40563
30. Müller SJ, Fabry B, Gekle S (2023) Predicting cell stress and strain during extrusion bioprinting. Phys Rev Appl 19:064061. https://doi.org/10.1103/PhysRevApplied.19.064061
31. Conti M, Santesarti G, Scocozza F, Marino M (2022) Chapter 6–models and simulations as enabling technologies for bioprinting process design. In: Conti M, Marino M (eds) Bioprinting: from multidisciplinary design to emerging opportunities. Academic Press, London (United Kingdom), pp 137–206. https://doi.org/10.1016/B978-0-323-85430-6.00009-1
32. Li M, Tian X, Schreyer D, Chen X (2011) Effect of needle geometry on flow rate and cell damage in the dispensing-based biofabrication process. Biotechnol Prog 27:1777–84. https://doi.org/10.1002/btpr.679
33. Nair K, Gandhi M, Khalil S, Yan K, Marcolongo M, Barbee K, Sun W (2009) Characterization of cell viability during bioprinting process. Biotechnol J 4:1168–77. https://doi.org/10.1002/biot.200900004
34. Chang R, Nam J, Sun W (2008) Effects of dispensing pressure and nozzle diameter on cell survival from solid freeform fabrication-based direct cell writing. Tissue Eng A 14:41–48. https://doi.org/10.1089/ten.a.2007.0004
35. Leppiniemi J, Lahtinen P, Paajanen A, Mahlberg R, Metsä-Kortelainen S, Pinomaa T, Pajari H, Vikholm-Lundin I, Pursula P, Hytönen VP (2017) 3d-printable bioactivated nanocellulose-alginate hydrogels. ACS Appl Mater Interfaces 9(26):21959–21970. https://doi.org/10.1021/acsami.7b02756
36. Batchelor GK (2000) An introduction to fluid dynamics. Cambridge University Press, Cambridge UK. https://doi.org/10.1017/CBO9780511800955
37. Bird RB, Armstrong RC, Hassager O (1987) Dynamics of polymeric liquids, vol 1: Fluid Mechanics, 2nd edn. Wiley, United States of America
38. Gallagher MT, Wain RAJ, Dari S, Whitty JP, Smith DJ (2019) Non-identifiability of parameters for a class of shear-thinning rheological models, with implications for haematological fluid dynamics. J Biomech 85:230–238. https://doi.org/10.1016/j.jbiomech.2019.01.036
39. Hospodiuk M, Moncal K, Dey M, Ozbolat I (2018) Extrusion-based biofabrication in tissue engineering and regenerative medicine. In: Ovsianikov A, Yoo J, Mironov V (eds) 3D printing and biofabrication. Springer, Cham, pp 255–281. https://doi.org/10.1007/978-3-319-45444-3_10
40. Gillispie G, Prim P, Copus J, Fisher J, Mikos AG, Yoo JJ, Atala A, Lee SJ (2020) Assessment methodologies for extrusion-based bioink printability. Biofabrication 12:022003. https://doi.org/10.1088/1758-5090/ab6f0d
41. Paxton N, Smolan W, Böck T, Melchels F, Groll J, Jungst T (2017) Proposal to assess printability of bioinks for extrusion-based bioprinting and evaluation of rheological properties governing bioprintability. Biofabrication 9:044107. https://doi.org/10.1088/1758-5090/aa8dd8
42. Blaeser A, Duarte Campos D, Puster U, Richtering W, Stevens M, Fischer H (2016) Controlling shear stress in 3d bioprinting is a key factor to balance printing resolution and stem cell integrity. Adv Healthc Mater 5:326–333. https://doi.org/10.1002/adhm.201500677
43. Matas J-P, Morris JF, Guazzelli E (2004) Inertial migration of rigid spherical particles in poiseuille flow. J Fluid Mech 515:171–195. https://doi.org/10.1017/S0022112004000254
44. Staben M, Davis R (2005) Particle transport in poiseuille flow in narrow channels. Int J Multiph Flow 31:529–547. https://doi.org/10.1016/j.ijmultiphaseflow.2004.12.004
45. Bhagat AA, Kuntaegowdanahalli S, Papautsky I (2008) Inertial microfluidics for continuous particle filtration and extraction. Microfluid Nanofluid 7:217–226. https://doi.org/10.1007/s10404-008-0377-2
46. Down L, Papavassiliou D, O'Rear E (2011) Significance of extensional stresses to red blood cell lysis in a shearing flow. Ann Biomed Eng 39:1632–42. https://doi.org/10.1007/s10439-011-0262-0

47. Bae Y, Jang H, Shin TH, Phukan G, Tran T, Lee G, Hwang WR, Kim J (2015) Microfluidic assessment of mechanical cell damage by extensional stress. Lab Chip 16:96–103. https://doi.org/10.1039/c5lc01006c
48. Korelc J, Wriggers P (2016) Automation of finite element methods. Springer, Switzerland. https://doi.org/10.1007/978-3-319-39005-5
49. Wriggers P (2008) Nonlinear finite element methods. Springer, Berlin, Heidelberg. https://doi.org/10.1007/978-3-540-71001-1
50. Buckingham E (1914) On physically similar systems; illustrations of the use of dimensional equations. Phys Rev 4:345–376. https://doi.org/10.1103/PhysRev.4.345
51. Nordson: Optimum Disposable Reservoir Systems. https://www.nordson.com/en/Products/EFD-Products/General-Purpose-Dispense-Tips Accessed 2023-01-23
52. Wu Q, Therriault D, Heuzey M-C (2018) Processing and properties of chitosan inks for 3d printing of hydrogel microstructures. ACS Biomater Sci Eng 4(7):2643–2652. https://doi.org/10.1021/acsbiomaterials.8b00415
53. Gaziano P, Marino M (2024) A phase-field model of cell motility in biodegradable hydrogel scaffolds for tissue engineering applications. Comput Mech 74(1):45–66. https://doi.org/10.1007/s00466-023-02422-8
54. Gaziano P, Marino M (2024) Computational modeling of cell motility and clusters formation in enzyme-sensitive hydrogels. Meccanica. https://doi.org/10.1007/s11012-024-01843-w